Modelling wing wake and tail-wake interaction of a clap-and-peel flapping-wing MAV

Armanini, Sophie; de Visser, Coen; de Croon, Guido; Aguiar Vieira Caetano, Joao

DOI
10.2514/6.2017-0581

Publication date
2017

Document Version
Accepted author manuscript

Published in
AIAA Modeling and Simulation Technologies Conference

Modelling wing wake and tail-wake interaction of a clap-and-peel flapping-wing MAV

Conference Paper · January 2017

DOI: 10.2514/6.2017-0581

4 authors:

Sophie Armanini
Delft University of Technology
14 PUBLICATIONS **11** CITATIONS
SEE PROFILE

João V. Caetano
Portuguese Air Force
15 PUBLICATIONS **59** CITATIONS
SEE PROFILE

Coen De Visser
Delft University of Technology
110 PUBLICATIONS **275** CITATIONS
SEE PROFILE

Guido de Croon
Delft University of Technology
116 PUBLICATIONS **643** CITATIONS
SEE PROFILE

This is an Accepted Manuscript of an article published in: AIAA Modeling and Simulation Technologies Conference 5-9 June 2017, Denver, Colorado. ISBN: 978-1-62410-491-6
Available online: https://arc.aiaa.org/doi/10.2514/6.2017-0581

Modelling wing wake and tail-wake interaction of a clap-and-peel flapping-wing MAV

S.F. Armanini* C.C. de Visser† G.C.H.E. de Croon†
Faculty of Aerospace Engineering, Delft University of Technology,2629HS Delft, The Netherlands
J.V. Caetano ‡
Portuguese Air Force Research Center, Sintra, Portugal

While tailless flapping-wing micro aerial vehicle designs are attracting significant interest, the tailed option offers many benefits, such as static stability and simpler control strategy, which separates the wing control from the tail control. However, the interaction between wing wake and tail is complex, due to the unsteady, time-varying wing aerodynamics, and is generally not modelled explicitly. We propose an approach to model the wing wake and wake-tail interaction in a tail-equipped flapping-wing robot. First, the wake is modelled as a periodic function depending on wing flap phase and position with respect to the wings. The overall model is constructed out of six low-order sub-models representing the mean, amplitude and phase of the velocity components considered. The parameters in each sub-model are estimated from PIV measurements using an identification method based on multivariate simplex splines. The computed model represents the measured wake with high accuracy, while being computationally manageable, and can be applied to different tail geometries within the range covered by the data. The wake model is then used within a standard aerodynamic force model, and combined with the effect of free-stream velocity, to estimate the forces produced by the tail. The obtained results provide a basis for further modelling and simulation work, and additionally yield insight into the role of the tail and its interaction with the wings in flapping-wing vehicles.

Nomenclature

A	=	Wave amplitude, with respect to the mean
Φ	=	Wave phase, s
$c_t(r)$	=	Tail chord at distance r from wing root, m
$C_{D,t}$	=	Tail drag coefficient
C_{d0}	=	Tail drag coefficient at 0° angle of attack
$C_{d\frac{\pi}{2}}$	=	Tail drag coefficient at 90° angle of attack
$C_{L,t}$	=	Tail lift coefficient
d	=	Model polynomial degree
d_c	=	Chordwise distance from considered point to wing trailing edge, m
d_s	=	Spanwise distance from considered point to wing root (fuselage), m
g	=	Acceleration due to gravity, $m \cdot s^{-2}$
m	=	Mass, kg
S_t	=	Tail surface area, m^2
t^*	=	Dimensionless time with respect to flapping period
t	=	Time instant, s
T	=	Flapping period, s

*PhD Candidate, Control and Simulation Section, Faculty of Aerospace Engineering, Delft University of Technology. AIAA Student Member.
†Assistant Professor, Control and Simulation Section, Faculty of Aerospace Engineering, Delft University of Technology. AIAA Member.
‡Researcher, Portuguese Air Force Research Center. AIAA Member.

V	=	Velocity norm, $m \cdot s^{-1}$
u, w	=	Velocity in x and z directions of corresponding frame, $m \cdot s^{-2}$
X, Z	=	Aerodynamic forces along body frame axes x_B and z_B, N
x_B, y_B, z_B	=	Unit axes of body reference frame
x_A, y_A, z_A	=	Unit axes of aerodynamic reference frame
$\mathbf{c}$	=	B-coefficient vector
b_{t_j}	=	Local barycentric coordinates with respect to simplex t_j
$\mathbf{B}$	=	Regressor matrix in barycentric coordinates
J	=	Number of simplices in triangulation
N	=	Number of measurements
$\mathbf{y}$	=	Model-predicted system output
$\mathbf{z}$	=	Measured system output
Greek		
α	=	Angle of attack, deg
f_f	=	Flapping frequency, Hz
ϵ	=	Least squares error
ρ	=	Air density $kg \cdot m^{-3}$
θ	=	Body pitch angle deg
$\hat{\Theta}$	=	Parameter estimates
ζ	=	Wing flap angle, deg
$\dot{\zeta}$	=	Wing flap angular velocity, $deg \cdot s^{-1}$
Subscripts		
A	=	Aerodynamic frame
B	=	Body Reference frame
loc	=	Local (pertaining to the blade element)
t	=	Tail
∞	=	Free-stream

I. Introduction

In nature many flapping-wing flyers operate taillessly. Thanks to elaborate wing actuation mechanisms they are able to achieve high-performance, efficient flight and stabilisation using only their wings. However, despite significant research into developing tailless flapping-wing robots,[?,?,?] many flapping-wing vehicles are still designed with a tail.[?,?,?,?] Tailed vehicles retain the advantage of more straightforward development and easier application. Furthermore, they benefit from both (a) the flapping wings – which provide high manoeuvrability, hover capability and enhanced lift generation, thanks to unsteady mechanisms – and (b) a conventional tail – providing static stability and simple control mechanisms. The combination of points (a) and (b) leads to overall favourable properties, as well as simpler design, modelling and implementation. The presence of a tail can be particularly advantageous for specific types of missions, e.g., where extended periods of flight are involved. Therefore, there is significant potential for such platforms. However, the simpler control and stabilisation mechanisms come at a price, as the interaction between tail and flapping wings must be considered, and this poses an additional challenge in the modelling and design process. The location of the tail behind the wings implies that the flow on the tail is significantly influenced by the flapping, with the downwash from the wings leading to a complex, time-varying flow on the tail.

Flapping-wing flight on its own is already highly challenging to model, due to the unsteady aerodynamics and complex kinematics. Significant effort has been spent on developing accurate aerodynamic models, particularly ones that are not excessively complex and can be applied for design, simulation and control. In an application context, the most widely used approach for this is simple, quasi-steady modelling,[?,?,?,?,?] and, to a lesser extent, data-driven modelling.[?,?,?,?,?,?] However, the combination of wings and tail has not been widely studied, despite being used on many flapping-wing robots; instead the design of the tail in such vehicles so far has largely relied on an engineering approach. Dynamic models either consider the vehicle as a whole without distinguishing between tail and wings,[?,?] or model the tail separately but without explicitly considering its interaction with the wings.[?] Not only is the wing-tail interaction highly complex, making a quasi-steady approach difficult but, additionally, only limited experimental data is available to support this type of analysis and potentially allow for data-driven approaches.

At present, no approach has been suggested specifically to model the forces on the tail in flapping-wing vehicles, particularly in a time-resolved perspective. A number of studies have analysed the wake behind flapping wings experimentally,[?] however modelling efforts have been scarce. Noteworthy among these, are the attempts to analyse the wake by means of actuator disk theory, adjusted to the flapping-wing case,[?,?] however this work mostly focuses on a cycle-averaged level and on analysis of the wing aerodynamics. A time-averaged result considering a single value for the wing-induced velocity is unlikely to capture the time-varying forces on the tail. On the other hand, a high-fidelity representation accounting for the unsteady effects that are present would require highly complex models that may not be suitable for practical purposes, e.g. CFD-based models. In practice, an intermediate solution is required, providing sufficient accuracy without excessive complexity.

This paper proposes a simple approach to model the wake of the wing of a flapping-wing robot, and thence the time-varying aerodynamics of the vehicle's tail, starting from wind tunnel data. The model is based on experimental observations, thus ensuring closeness to the real system, but avoids excessive complexity to allow for simulation and control applications. The modelling process comprises two steps: firstly, a model is developed for the flapping-wing wake, depending on the wing motion. The wake is represented as a periodic function, where the velocity at each position in the considered range depends on the position itself in relation to the wings, as well as on the wing flapping phase. The overall wake model is constructed out of six low-order sub-models representing the mean, amplitude and phase of the two velocity components considered, with the parameters in each sub-model being estimated from PIV measurements. Secondly, the obtained wake model is used to compute the flapping-induced velocity experienced by the tail, considering the tail positioning and geometry, and incorporated in a standard aerodynamic force model to estimate the forces produced by the tail. Tail forces are predicted for different flight conditions, also considering the effect of free-stream velocity in forward flight. Aerodynamic coefficients are based on quasi-steady flapping wing aerodynamic theory, as the tail experiences a time-varying flow, similar to what it would experience if it were itself performing a flapping motion.

The obtained results provide a basis for advanced modelling and simulation work, and additionally yield new insight into the role of the tail and its interaction with the wings in flapping-wing vehicles. The latter will be valuable for improved tailed FWMAV designs, as well as supporting the development of tailless vehicles in the future. Combining the resulting model with a model of the flapping wings will result in a full representation of the studied vehicle, constituting a useful basis for development of a full simulation framework, and supporting novel controller development.

The rest of this paper is structured as follows. Section II provides an overview of the experimental data. Section III briefly outlines the overall modelling approach. Detailed explanation of the wing wake modelling, starting from analysis of the experimental data, is given in Section IV, while the model identification and results are discussed in Section V. The proposed tail force model is presented in Section VI. Section VII closes with the main conclusions.

II. Experimental data

The modelling approach suggested is based on experimental data collected on a robotic test platform. Stereo-PIV data were used to model the flapping-wing induced velocity on the tail. The test platform and experimental data are presented in the remainder of this section.

II.A. Test platform

The flapping-wing micro aerial vehicle (FWMAV) used in this study, shown in Fig. 1, is a 18g, four-winged FWMAV capable of free-flight in conditions ranging from hover to fast forward velocities up to 7m/s, with flapping frequencies of 10Hz to 14Hz. The wings have a biplane, 'X' configuration, which enhances lift production thanks to the unsteady clap-and-peel mechanism, and the upper and lower wing leading edges on either side meet at a dihedral of 13°. The inverted 'T' styrofoam tail provides static stability and allows for simple, conventional control mechanisms, that can be separated from the wing-flapping. As such, the tail is an essential element of the current design. Further details on the FWMAV can be found in Ref. ?.

II.B. Time-resolved PIV measurements

To obtain insight into the wake behind the flapping wings and model it, a set of previously collected stereo-PIV measurements[?] was used. These measurements were conducted at two different flapping frequencies (9.3Hz and 11.3Hz), at 0m/s free-stream velocity (representing hover conditions), to obtain the 2D velocity profile in the wake of the flapping wings. The experimental setup is shown in Fig. 2. Subfigure 2(a) indicates the positioning of the three high-speed cameras (Photron FASTCAM, SA 1.1), which allowed for the wing flap angle corresponding to each PIV image to be obtained in addition to the velocity vectors. The figure also clarifies the coordinate frame used as a reference in the wake measurements.

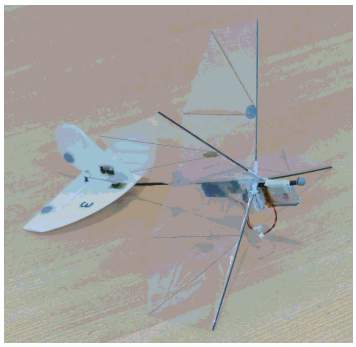

Figure 1: Flapping-wing robot used in this study (DelFly II[?])

Data were obtained at ten different spanwise positions (d_{plane}) to the right hand side of the fuselage, covering a range from 20mm to 200mm, in steps of 20mm. At each spanwise position, measurements were conducted in a 240mm×240mm chordwise oriented plane (aligned with the vehicle's XZ plane), positioned 10mm downstream of the wing trailing edges, as clarified by Fig. 2. The planes were each centred around an axis 24mm above the fuselage, in order to capture the full wing stroke amplitude, considering the 13° wing dihedral of the platform. Double-frame images were captured at a recording rate of 200 Hz, and approximately 30-36 flap cycles (depending on the flapping frequency) were captured at each position. The post-processing[?] resulted in a spacing between measurement points of approximately 3.6mm in each direction. Measurements in the region closest to the wings were found to be unreliable due to laser reflection, hence data acquired in the 60mm of the measurement plane closest to the wings were discarded. Details on the PIV measurements, experimental setup and pre and post processing can be found in Ref. ?.

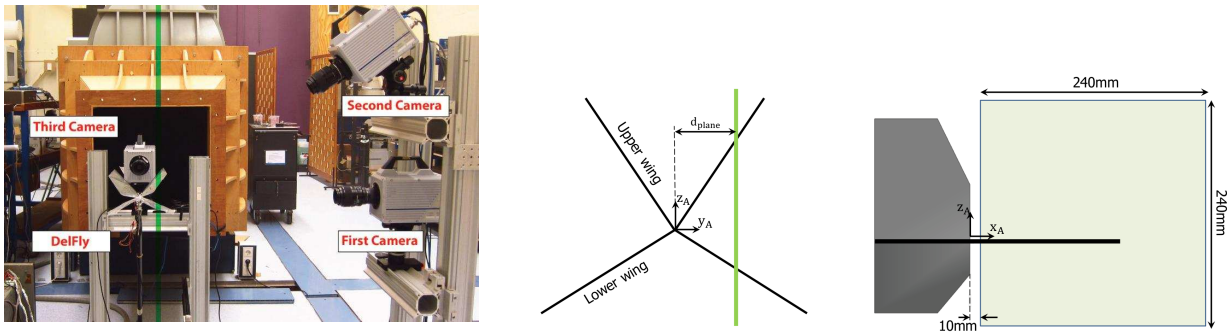

(a) Photograph of the setup (b) Front view (c) Side view

Figure 2: Experimental setup for PIV measurements; figures adapted from[?]

III. Modelling approach overview

We begin by considering a highly simplified aerodynamic model, where the tail lift and drag are assumed to be described by the standard equations,

$$L_t = \frac{1}{2}\rho S_t V_t^2 C_{Lt}(\alpha_t) \tag{1}$$

$$D_t = \frac{1}{2}\rho S_t V_t^2 C_{Dt}(\alpha_t) \tag{2}$$

where ρ is the air density, S_t is the tail reference area, V_t is the flow velocity, α_t is the angle of attack (AOA), and C_{Lt} and C_{Dt} are the lift and drag coefficients of the tail, respectively.

The AOA and velocity experienced by the tail are significantly affected by the downwash from the flapping wings. As a consequence, they are time-varying and complex, and depend on both the wing kinematics, and the free-stream conditions. Additionally, the velocity and AOA perceived by the tail vary depending on the

spanwise location that is considered, which justifies a blade element modelling approach, using differential formulations of Eqs. 1–2. The local AOA and velocity experienced at each blade element can be expressed as follows:

$$\alpha_{t,loc} = arctan\left(\frac{-w_{t,loc}}{u_{t,loc}}\right) \tag{3}$$

$$V_{t,loc} = \sqrt{u_{t,loc}^2 + w_{t,loc}^2} \tag{4}$$

where u and w are the x and z components of the local velocity perceived by the tail blade element, according to the coordinate frame defined in Fig. 2. Each component includes the contribution of the free-stream velocity (V_∞), as well as the contribution of the wing flapping-induced velocity at the spanwise position considered.

Since the free-stream contribution can be approximately computed from the flight conditions, the main unknown is the contribution of the wings. A realistic model of the aerodynamics of a tail positioned behind flapping wings requires representing the time-varying velocity profile that results from the unsteady wing aerodynamics. As a result, the first step in the modelling process is to represent the flapping-wing wake and deduce the resulting effective velocity and AOA on the tail. The second step is, then, to include the induced velocity predicted by the aforementioned model in the differential form of Eqs. 1 and 2. Additionally, there may be further effects that result specifically from the interaction of the free-stream and wake components: these require experimental data to be quantified, and are excluded at this stage.

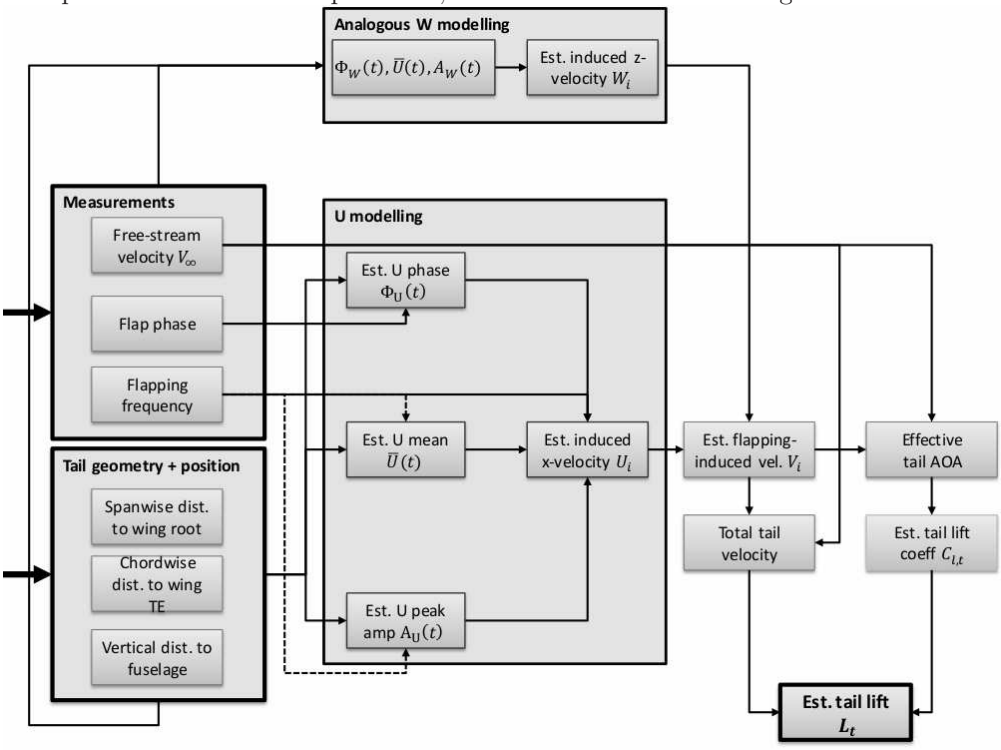

Figure 3: Diagram illustrating the overall modelling approach developed.

Further details on the modelling process are provided in the following sections, while the overall modelling approach is clarified by the diagram in Fig. 3. Throughout the rest of this text, this diagram will serve as a reference.

IV. Wing wake modelling

IV.A. Experimental evaluation of the wing wake

The velocity perceived by the tail in flapping-wing vehicles consists of a combination of free-stream velocity and induced velocity from the wings. The latter component imparts a time-varying behaviour to the tail, and is of particular interest because at the typical flight velocities of the FWMAV considered, the induced

velocity is of a comparable order of magnitude to the free-stream velocity. Prior to modelling, the PIV data was analysed to establish the main trends and derive a suitable modelling approach.

Whilst initially all available measurements were considered, finally the focus was placed on the ones relevant for the current tail configuration and possible variations from it. Therefore, only these data were used to model the wake, as shown in Fig. 4. In spanwise (y_A in Fig. 2) direction, data collected at distances up to 85mm from the fuselage impinge upon the current tail design. As larger spans are being considered for future designs, data up to 100mm from the wing root were considered. Based on analogous considerations, in x_A direction, the domain of interest was reduced to the first 150mm after the wing trailing edges.

In z_B direction, data for a small range of values above and below the fuselage were evaluated, to gain an idea of the variation in this direction (cf. Fig. 8). Although the tail essentially remains within approximately the same plane, it was considered useful to consider such changes because the tail has a thickness, and its position may vary slightly with respect to the static case due to vibrations and bending of the fuselage during flight.

An initial assessment of the data allowed for the following observations. Firstly, it was found that the induced velocity in x_A direction (u) is the main contributor to the average wake velocity, while the mean w velocities are much smaller, often close to zero (cf. Fig. 5). However, both components display significant oscillations during the flap cycle and hence both should be considered in a time-resolved model. The oscillations in w velocity also influence the local AOA on the tail.

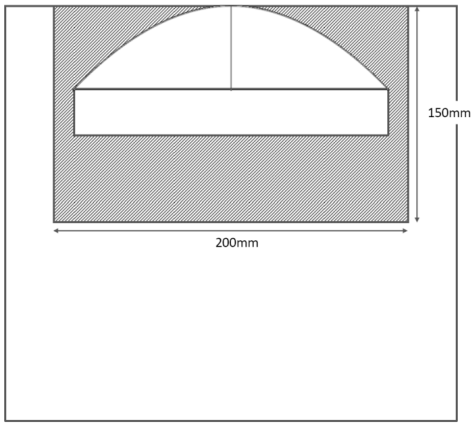

Figure 4: Main tail geometric features and position, and area covered by the wake model, in relation to the original region covered by the PIV measurements.

Secondly, both the time histories (cf. Figs. 5, 6) and the Fourier transforms of the measurements show that the wake is predominantly periodic and at fixed positions in the wake there is considerable agreement between separate flap cycles. This suggests that the velocities can be directly related to the wing flapping. Nonetheless, at some positions in the wake, the data become less clean and display more variation between cycles. The spatial distribution of these abnormal measurements in the wake suggests that unsteady effects such as vortices may be occurring. A model accounting for these effects would easily become highly complex, hence for the current study the wake is assumed to be periodic. This still captures the main effects observed, while yielding simpler and more interpretable results.

Thirdly, it was found that in most of the domain relevant for the tail, the frequency content is largely concentrated at the flapping frequency (cf. Fig.7). Thus, it was considered acceptable for a first approximation of the velocities on the tail, to low-pass filter the data just above the flapping frequency. Nonetheless, there are isolated parts of the wake where this assumption becomes questionable, e.g., very close to both the wing trailing edges and the wing root. These are the same locations mentioned in the previous point, where measurements are likely affected by unsteady effects. At these locations, it was also observed that the frequency content shifts towards higher harmonics. This cannot be captured by the current model, but should be considered in future work.

As the velocities are mostly periodic, the amplitude and phase of the oscillations were considered next. Figs 9 and 5 show that there are trends in the peak amplitude and phase of the wake velocity, with both the chordwise distance from the wing trailing edges, and the spanwise distance from the fuselage. The measurements obtained very close to both the wing root and the wing trailing edge are often less clean than those obtained elsewhere, possibly due to the complex aerodynamics resulting from the vicinity of the upper and lower wings to each other and their mutual interference. Similarly, the data obtained directly behind the wing tips are chaotic and only barely periodic, presumably due to the complex aerodynamics behind the wing tips – however for the current FWMAV it is unlikely that even new tail designs would be as wide as the wings. Due to the described effects, the clearest measurements were obtained at intermediate spanwise distances, away from both the wing root and the wing tip, with some exceptions due to unsteady effects mentioned in the previous paragraphs. It is interesting to note that generally the u velocities decrease with

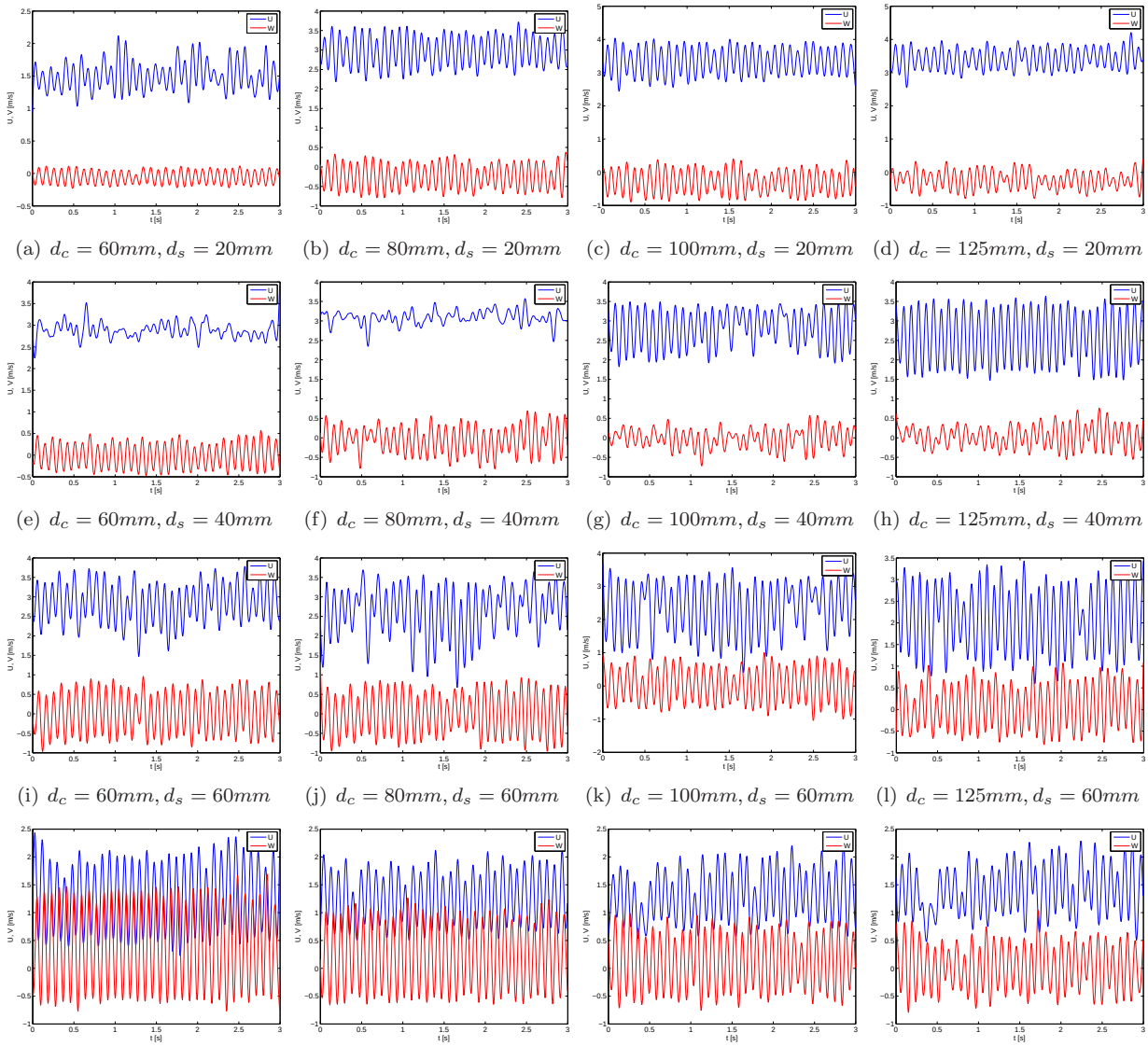

(a) $d_c = 60mm, d_s = 20mm$ (b) $d_c = 80mm, d_s = 20mm$ (c) $d_c = 100mm, d_s = 20mm$ (d) $d_c = 125mm, d_s = 20mm$

(e) $d_c = 60mm, d_s = 40mm$ (f) $d_c = 80mm, d_s = 40mm$ (g) $d_c = 100mm, d_s = 40mm$ (h) $d_c = 125mm, d_s = 40mm$

(i) $d_c = 60mm, d_s = 60mm$ (j) $d_c = 80mm, d_s = 60mm$ (k) $d_c = 100mm, d_s = 60mm$ (l) $d_c = 125mm, d_s = 60mm$

(m) $d_c = 60mm, d_s = 100mm$ (n) $d_c = 80mm, d_s = 100mm$ (o) $d_c = 100mm, d_s = 100mm$ (p) $d_c = 125mm, d_s = 100mm$

Figure 5: Measured wake u and w flow velocities at different chordwise (d_c) and spanwise (d_s) distances.

spanwise distance. This may be related to the specific vortex formations, but may also be enhanced by the dihedral of the wings. As the tail is aligned with the fuselage, at increasing spanwise distances from the wing root, the tail plane is increasingly less influenced by the main vortex formations.

In chordwise direction, mean u values generally decrease farther away from the wing trailing edges, with the extent of this decrease varying depending on the spanwise position, while w average velocities remain close to zero and display less clear trends. At large distances from the trailing edges, the peaks are small and tend to merge together, which complicates the recognition of patterns. This effect is further enhanced by the PIV settings, typically chosen so as to capture the highest velocity in the measurement plane effectively, to the detriment of lower velocities occurring simultaneously at other locations. In vertical (z_B) direction, changes were found to be small but noticeable in the mean u values, but only minor in the peak amplitudes (cf. Fig. 8) and w velocities.

Comparing the data obtained at the two different flapping frequencies suggests that a higher flapping frequency leads to a higher mean velocity (mainly u), while not significantly affecting the time-varying component. However, the availability of data for only two different flapping frequencies was considered insufficient for reliable conclusions to be drawn, hence this likely dependency was not further considered in

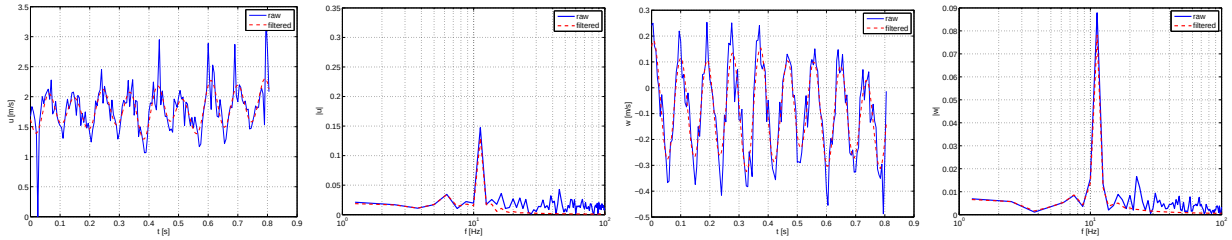

(a) u, time domain (b) u, frequency domain (c) w, time domain (d) w, frequency domain

Figure 7: Example of the effect of low-pass filtering just above the flapping frequency ($\sim 12Hz$), in the time and frequency domain (wake position shown: $d_s = 20mm, d_c = 77mm$).

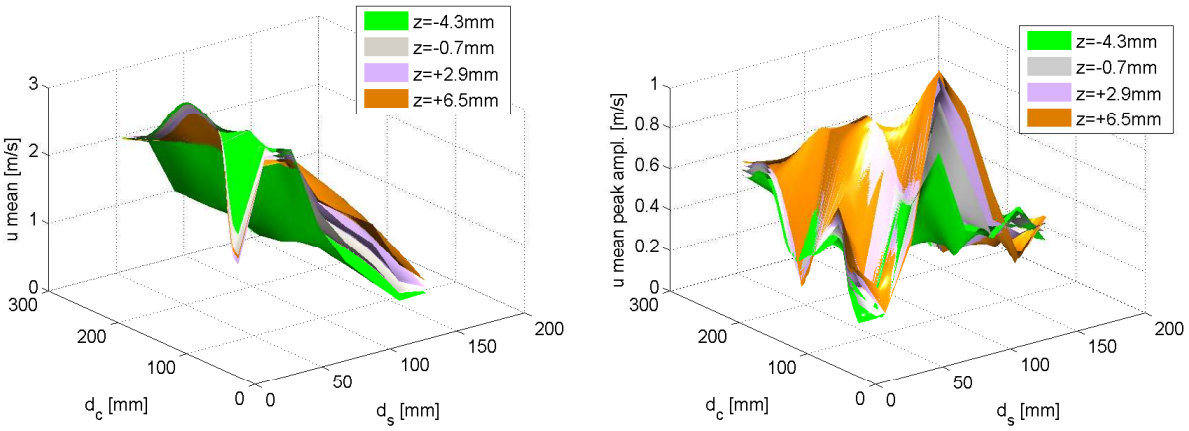

(a) (b)

Figure 8: Velocity component u (mean and peak amplitude) obtained at different spanwise and chordwise positions, for 4 different vertical positions (z).

the modelling process, at this stage. Contrasting the PIV measurements for different flapping frequencies also reveals similar overall trends, suggesting a degree of reliability. In general, it should be considered that while a full aerodynamic interpretation requires extensive 3D data and analysis beyond the scope of this study, the unsteady processes involved imply that the observed trends may not always be intuitive. In this sense, the aforementioned similarity is a particularly useful indication.

The wing wake modelling approach was based on the preceding discussion and is outlined in the following section.

IV.B. Preliminary assumptions

The following assumptions and simplifications were made within the modelling process.

Firstly, based on the discussion in Sec. IV.A, the wing wake was assumed to be periodic. As mentioned previously, this is not always the case, nonetheless, even where there are additional effects, the periodic component remains significant, such that this assumption was considered acceptable for a first approximation.

Secondly, based on the frequency content analysis of the PIV data, it was decided to filter the wake velocities just above the first flapping harmonic.

Thirdly, the wing beat was assumed to be sinusoidal. While in the considered FWMAV the outstroke is slightly slower than the instroke, this difference is small and was considered negligible, particularly in view of the highly simplified nature of the aerodynamic model itself. More accurate mathematical representations of the kinematics, e.g. using a split cycle piecewise representation,[?] or different functions such as the hyperbolic tangen would have increased the model complexity and interpretability, and are left for future work.

Fourthly, velocities in y_B (or y_A) direction were assumed to be negligible. Given that the platform is symmetrical around the x_B and y_B axes, the contribution of this component should be minor. Moreover, no

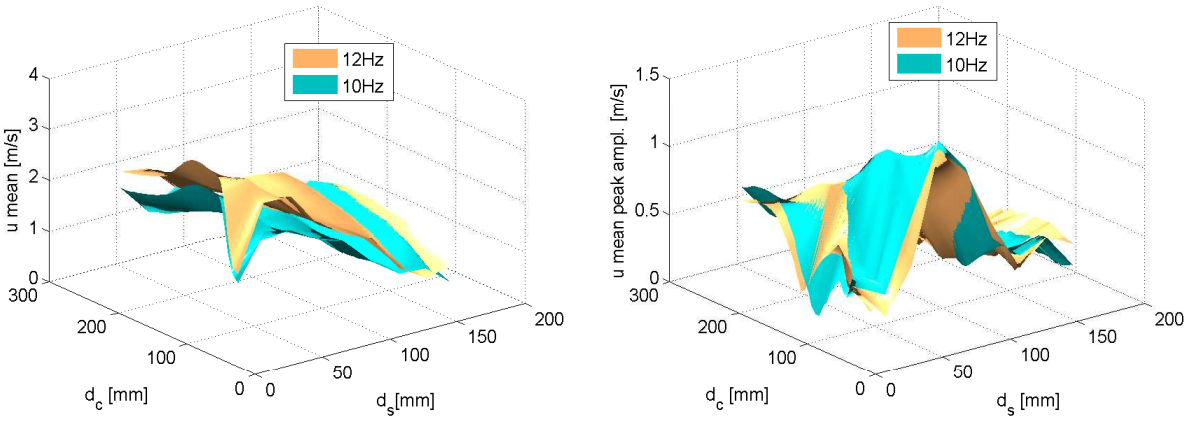

(a) (b)

Figure 9: Velocity component u (mean and mean peak amplitude) obtained at different spanwise and chordwise positions and fixed vertical position, for 2 different flapping frequencies.

PIV data were available for this component.

Finally, as a clarification: the wake models developed in this section predict the velocity *of the flow*, according to the coordinate system A shown in Fig. 2. The velocity that will be used to determine the tail forces in the subsequent section, is the velocity *of the respective tail section*, according to the coordinate system shown in Fig. 2. As the x and z axes of the two systems are reversed (rotation by π about the y axis), the u and w components of the tail velocity have the same sign as the corresponding components of the flow velocity.

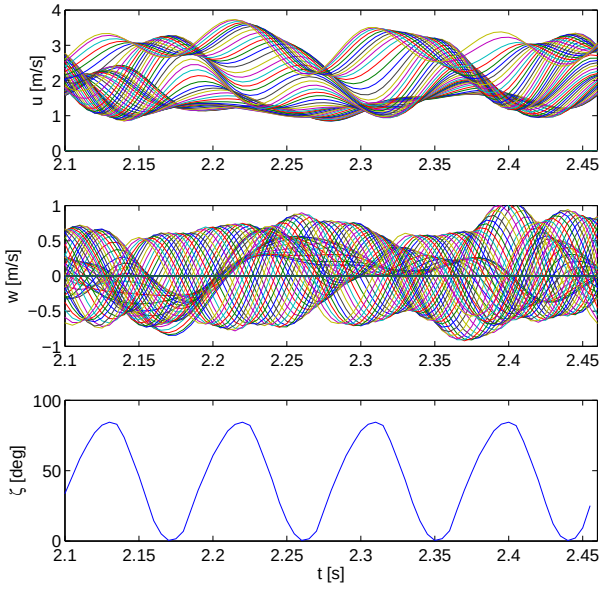

Figure 6: Overlapped measurements for velocity components u and w obtained at different chordwise positions, at a fixed vertical position (approximately in the plane of the tail), for a spanwise position $d_s = 60mm$.

IV.C. Sinusoidal model structure of the wing wake

The two components of the wake velocity (u, w) were approximated as cosine waves:

$$\hat{u}(d_s, d_c, \zeta) = \hat{\bar{u}} + \hat{A}_u(d_s, d_c)\cos\left(\Phi_u(d_s, d_c, \zeta)\right) \tag{5}$$

$$\hat{w}(d_s, d_c, \zeta) = \hat{\bar{w}} + \hat{A}_w(d_s, d_c)\cos\left(\Phi_w(d_s, d_c, \zeta)\right) \tag{6}$$

where d_c is the chordwise distance from the wing trailing edges, d_s is the spanwise distance from the wing root and ζ is the instantaneous wing flap angle. The unknown parameters in the above model are: the mean velocities $(\bar{u}, \bar{w})$, the amplitudes of the oscillatory peaks with respect to the mean $(\hat{A_u}, \hat{A_w})$, and the phases with respect to the wing flap phase (Φ_u, Φ_w). Each parameter must be known at any position in the wake, within the range considered (cf. Fig. 4).

The phase of the induced velocities, in particular, must also be related to the wing flap phase, so that an accurate time-resolved model is obtained, that can predict the velocities at any moment of the flap cycle.

As mentioned previously, the wing flapping of the test platform is assumed to be sinusoidal. The magnitude of the angle of each wing with respect to the dihedral can thus be written as,

$$\zeta := \bar{\zeta} + A_\zeta \cos(2\pi t^*) \tag{7}$$

If the beginning of the flap cycle is considered the moment when the wings are open, the phase corresponds to that of a pure cosine wave. The induced velocities are then waves with the same frequency as the wing flap angle, but phase shifted with respect to it. Φ_u and Φ_w in Eq. 5 can be formulated as,

$$\Phi_{u,w} = (2\pi(t^* + \Delta t_{u,w} f_f)) \tag{8}$$

where t^* is nondimensional time with respect to the wing flapping, t is dimensional time, and f_f is flapping frequency. Δt is the time difference between the start of the peak (assumed to occur when the wings are open) and the time at which the peak of the considered wake velocity component occurs.

Applying this formulation requires knowing the time within the flap cycle (t^*). In practice, one possibility to do this is to use a sensor to register when the wings are at a particular position, measure the time with respect to this instant, and reset to zero every time the wings return to this position. If the flapping frequency is known, the nondimensional time can be calculated, and the above equations can be applied once the time shift Δt is determined. An alternative is to find a function relating flap time to wing flap angle, and measuring the flap angle at each instant. As the same angles occur twice per cycle, the result is a piecewise function that also depends on the flap rate. Either way, it can be assumed that the time with respect to the wing flapping is known or measurable.

The relation of each of the six parameters in Eqs. 5 and 6 with position in the wake (d_c, d_s) and flap phase was estimated from the PIV data presented in Sec. II.B. This is discussed in the subsequent section. It should be noted that the parameters are likely to also depend on the flapping frequency, however this dependence cannot be determined conclusively with the current data, which only cover two different flapping frequencies. At present, results were determined only for the specific flapping frequencies for which data were available. As the procedure is analogous for different flapping frequencies, results are only presented for the 11.2Hz case.

V. Model identification and results

V.A. Sub-model identification

The unknown parameters $(\bar{u}, A_u, \Phi_u, \bar{w}, A_w, \Phi_w)$ in Eq. 5 (hereafter 'wake parameters') were determined from the PIV data presented in Sec. II.B using an identification method. In particular, a separate sub-model was developed to estimate each of the six original parameters (cf. Fig. 3). In an identification context, each of the wake parameters is therefore the output (z) of a separate sub-model. In view of the assumed wake periodicity, rather than using all measurements, the measured output at each wake position and nondimensional time instant was defined as the mean over all flap cycles recorded at that particular position and time. Data for ten flap cycles were used to construct these models, to allow for validation of the results with the remaining data. Moreover, as discussed in Sec. IV.A, changes of the velocities in z_A direction are small but visible, and should be included in the model. Thus, instead of using measurements for the single particular z_A position closest to the tail plane, we computed the average of the velocities measured at the two closest measurement points above and below the tail plane. This covers a distance of approximately 8mm and should improve the reliability of the final force model results. Given the small magnitude and gradualness of the variation observed in this direction (cf. Fig. 8), using a larger number of points is not expected to change the results significantly.

As seen in Sec. IV.A, the wake parameters depend nonlinearly on chordwise and spanwise position with respect to the wings, and on the wing flap phase, hence the sub-models must depend on these variables. To obtain low-order models that nonetheless can represent these dependencies accurately, an identification method based on multivariate simplex B-splines was chosen. This allows for accurate global models to be obtained by combining low-order local ones, thus avoiding the typically high model orders required to cover the entire domain of a nonlinear system with a single polynomial model. A thorough explanation of the estimation method can be found in Refs. **?**, **?**, hence only a concise overview is given here.

Simplex splines are geometric structures minimally spanning a set of n dimensions. Each simplex t_j has its own local barycentric coordinate system, and supports a polynomial that can be written (in so-called

B-form) as,

$$p(x) = \sum_{|\kappa|=d} c_{\kappa}^{t_j} B_{\kappa}^{d}(b_{t_j}(x)), x \in t_j \tag{9}$$

where $c_{\kappa}^{t_j}$ are the coefficients of the polynomial, known as B-coefficients, b_{t_j} are the barycentric coordinates of point x with respect to simplex t_j, d is the degree of the polynomial, $\kappa = (\kappa_0, \kappa_1, \ldots, \kappa_n)$ is a multi-index containing all permutations that sum up to d, and $B_{\kappa}^{d}(b)$ are the basis functions of the multivariate spline:

$$B_{\kappa}^{d}(b) := \frac{d!}{\kappa!} b^{\kappa}, \quad d \geq 0, \kappa \in N \tag{10}$$

Polynomials of the form given in Eq. 9 can be used as a model structure for system identification. The underlying idea is that prior to estimation, the identification domain is divided into a net of non-overlapping simplices (triangulation), and a separate local model is identified for each simplex, using the datapoints contained in that simplex. In an identification framework, the basis functions in Eq. 9 represent the measurements used to model the chosen system output, whereas the B-coefficients are the model parameters to be estimated and locally control the structure of the polynomial.

In this study, an ordinary least squares estimator was used,[?] hence, the output equation at each measurement point i is,

$$z_i = \sum_{|\kappa|=d} c_{\kappa}^{t_j} B_{\kappa}^{d}(b_{t_j}(x_i)) + \epsilon_i, x \in t_j \tag{11}$$

or in vector form,

$$\mathbf{z} = \mathbf{B}\mathbf{c} + \epsilon. \tag{12}$$

The $\mathbf{B}$ matrix in the above equation contains the regressor measurements, converted to the barycentric coordinates of the simplex containing them. As each local model is constructed using only the data within a single simplex, the global B-matrix for the full triangulation is a block diagonal matrix constructed from the B-matrices of the J simplices.

$$\mathbf{B}_{glob} = diag(\mathbf{B}_{t1}, \ldots, \mathbf{B}_{tJ}) \tag{13}$$

Given the B-matrix, an OLS estimator can be defined for the B-coefficients in $\mathbf{c}$.

$$\hat{\mathbf{c}} = (\mathbf{B}^T\mathbf{B})^{-1}\mathbf{y}. \tag{14}$$

To ensure continuity between the separate models, continuity conditions of the following form can be defined between neighbouring simplices,

$$\mathbf{H} \cdot \mathbf{c} = \mathbf{0} \tag{15}$$

where H is the smoothness matrix defining the continuity conditions. The estimator can then be reformulated to include these continuity conditions, e.g. as explained in Ref. ?.

The outlined approach was applied to estimate a model for each of the six wake parameters in Eq. 5, leading to six separate sub-models, that are finally combined to estimate the total time-resolved induced velocity components, as shown in Fig. 3. The output variable for each sub-model is thus one of the aforementioned parameters. In each case, an appropriate model structure and triangulation of the domain defined by the chordwise and spanwise positions in the wake were chosen, based on analysis of the input-output data. The chosen modelling setup for each case is shown in Tab. 2. In all cases, equally shaped and evenly distributed two-dimensional simplices were used. When comparable results were obtainable with different combinations of model order and triangulation density, the solution leading to the lowest model order was favoured, as it leads to a comparatively smaller number of coefficients and is less prone to numerical issues. Zero-order continuity was considered sufficient at this stage, as the intended usage of the model does not require more.

Note that in the case of the phase, to facilitate the modelling, the time delay was formulated in a continuous way: starting from the time delay of the earliest occurring peak in the wake, other peaks are taken incrementally, going over into successive cycles, rather than restarting at zero when the delay becomes larger than the cycle period. However, in practice it is useful to know where the peaks in the wake are located at a particular moment in the (current) flap cycle, rather than with respect to the same particular flap cycle that may be more than one flapping period away. Thus, in a second moment, when going from the wave parameters to the actual wave, the phase model results were transformed back into the relative frame of a single flap cycle, to yield the relative time delay with respect to the most recent peak.

$$\Delta t_{rel} = \Delta t_{abs} \mod T_{cycle} \tag{16}$$

where T_{cycle} is the flapping period.

Table 2: Modelling parameters for each output variable and performance of the resulting model

output	model deg.	continuity	# simplices	RMS	R^2
$\bar{u}$	2	0	8	0.05m/s	1.0
A_u	4	0	4	0.01m/s	1.0
Φ_u	2	0	8	0.002s	1.0
$\bar{w}$	2	0	8	0.01m/s	1.0
A_w	2	0	8	0.01m/s	1.0
Φ_w	2	0	2	0.003s	0.98

V.B. Wake modelling results

The obtained results are summarised in Figs. 10–15. It can be seen that in general the respective models represent the PIV-computed wake parameters with significant accuracy, mostly leading to small residuals and high R^2 values (cf. Tab. 2 and Figs. 10–15). The residuals generally tend to be larger close to the wing root, in agreement with the observations made earlier regarding more unsteady regions in the wake, where trends are more nonlinear. Nonetheless, even at these locations, the residuals remain small and the model accuracy high.

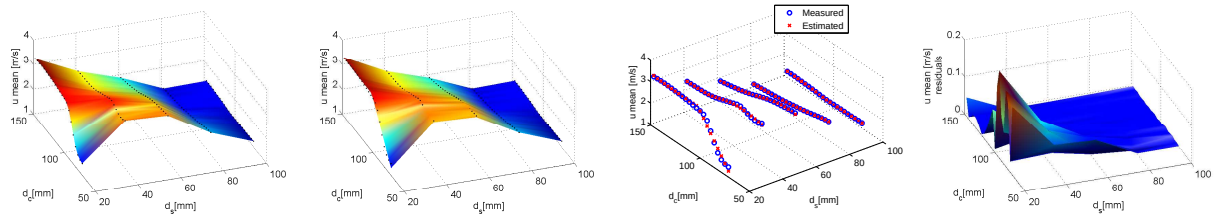

(a) Measured data surface (b) Model surface (c) Measured and model-predicted output (d) Residual surface

Figure 10: Model: u mean parameter

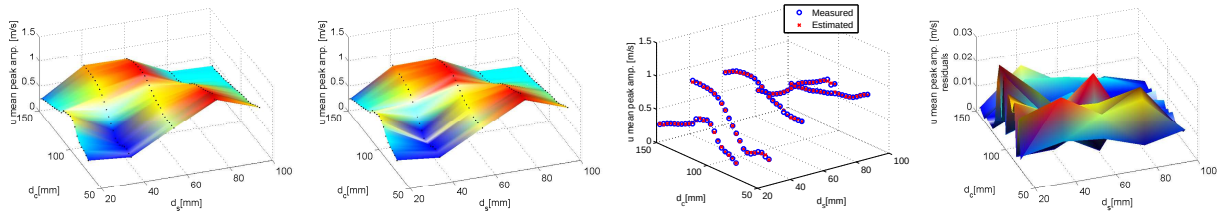

(a) Measured data surface (b) Model surface (c) Measured and model-predicted output (d) Residual surface

Figure 11: Model: u peak amplitude parameter

Evidently, however, the ultimate goal is to represent the actual wake velocities, and hence to evaluate the extent to which the suggested sinusoidal approximation of Eqs. 5–6 is itself acceptable. As observed in Sec. IV.A, the PIV data are dominantly periodic, and in some cases close to a perfect sine wave, but not always. Hence, a further evaluation of the obtained wake model was made by substituting the estimated parameters (i.e. the predicted output of the six sub-models) into Eq. 5 to compute the velocities as each considered position in the wake, and comparing the outcome to the direct PIV measurements. In particular, the PIV data used in this evaluation were not used in the identification process, hence this comparison constitutes a validation of the wake model.

Fig. 16 shows several examples of the model validation process. It can be observed that, as expected from the PIV data and the highly accurate estimates of the wake parameters, the agreement is generally significant, especially in mean and amplitude, which are mostly very close to those of the data. The amplitude displays some discrepancies, mostly related to the modelling assumption of periodicity, which, as discussed previously, is not always fully valid, rather than to the identified model itself. As discussed in Sec. IV.A, these assumptions are particularly questionable close to the wings – this can for instance be seen in the less accurate result obtained in Subfigs. (e)–(h). Overall, the most notable discrepancies are found in the

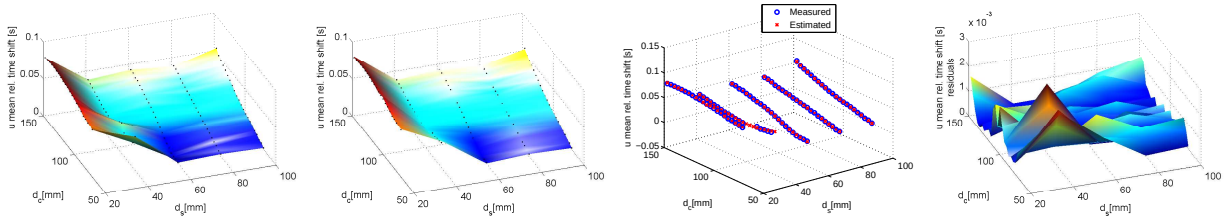

(a) Measured data surface (b) Model surface (c) Measured and model-predicted output (d) Residual surface

Figure 12: Model: u phase delay parameter

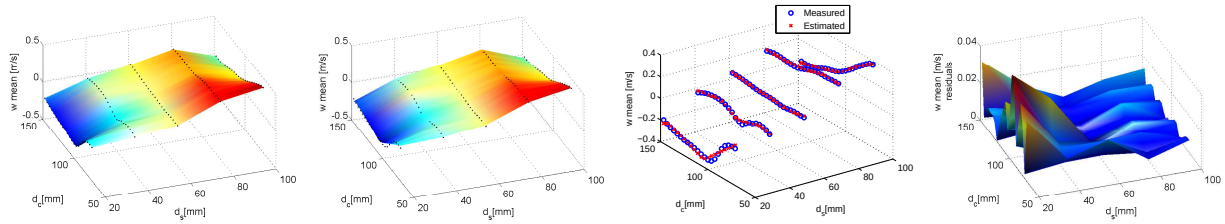

(a) Measured data surface (b) Model surface (c) Measured and model-predicted output (d) Residual surface

Figure 13: Model: w mean parameter

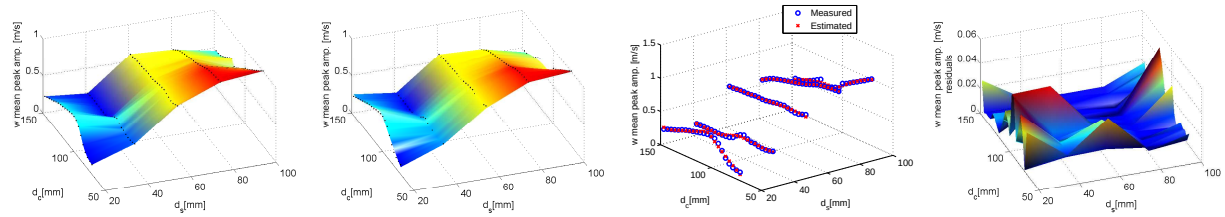

(a) Measured data surface (b) Model surface (c) Measured and model-predicted output (d) Residual surface

Figure 14: Model: w peak amplitude parameter

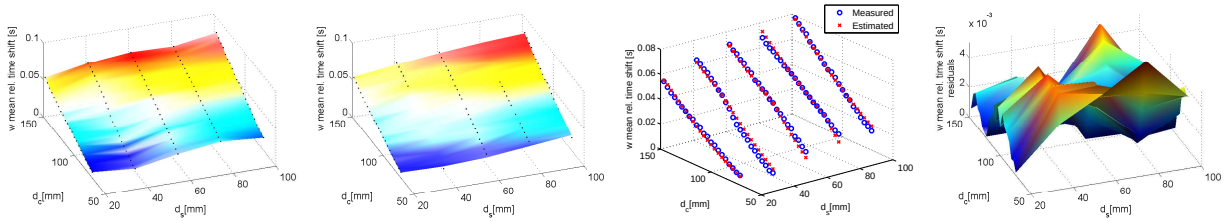

(a) Measured data surface (b) Model surface (c) Measured and model-predicted output (d) Residual surface

Figure 15: Model: w phase delay parameter

phase, which in some cases is not fully in agreement, as seen in Fig. 16. This may be a result of insufficient accuracy in determining the flapping frequency, which in some cases varies slightly throughout the data samples. Indeed, it appears that the frequency itself is not always identical, rather than the phase delay. As a small discrepancy in phase may add up to a large error over time, it is especially important that the frequency is determined accurately, and this should be ensured when applying this model.

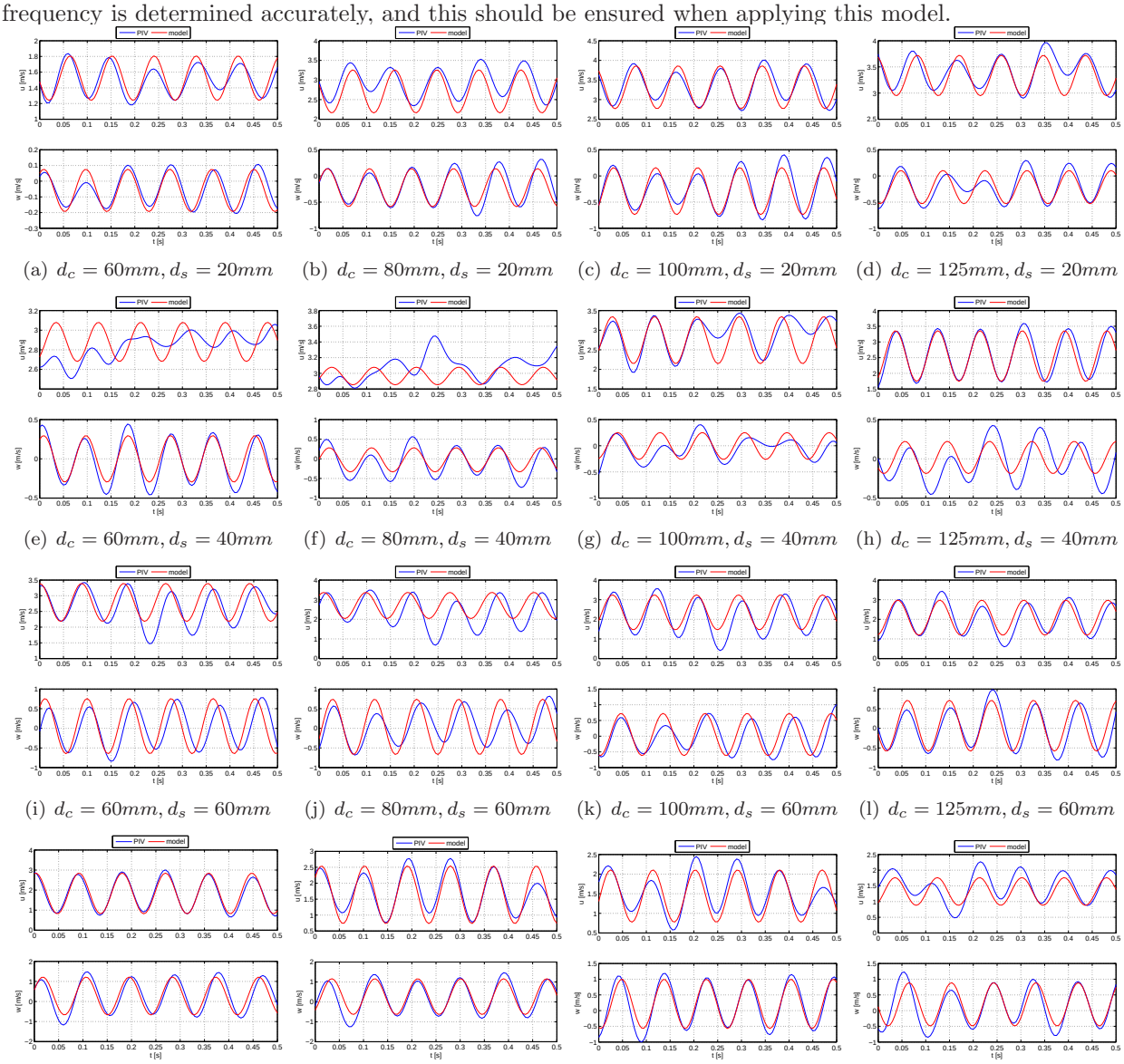

(a) $d_c = 60mm, d_s = 20mm$ (b) $d_c = 80mm, d_s = 20mm$ (c) $d_c = 100mm, d_s = 20mm$ (d) $d_c = 125mm, d_s = 20mm$

(e) $d_c = 60mm, d_s = 40mm$ (f) $d_c = 80mm, d_s = 40mm$ (g) $d_c = 100mm, d_s = 40mm$ (h) $d_c = 125mm, d_s = 40mm$

(i) $d_c = 60mm, d_s = 60mm$ (j) $d_c = 80mm, d_s = 60mm$ (k) $d_c = 100mm, d_s = 60mm$ (l) $d_c = 125mm, d_s = 60mm$

(m) $d_c = 60mm, d_s = 80mm$ (n) $d_c = 80mm, d_s = 80mm$ (o) $d_c = 100mm, d_s = 80mm$ (p) $d_c = 125mm, d_s = 80mm$

Figure 16: Validation example: model-predicted and measured wake velocities u and w at different wake locations, using Eq. 5 and the parameters estimated with the sub-models presented in Sec. IV.C.

On a final note, it should be considered that although a relatively large number of parameters (B-coefficients of the sub-models) is required to achieve sufficient accuracy over the entire domain considered, the model structure itself is based on low-order components and does not require heavy computations to implement. Additionally, applying the model the model for tail force estimation requires only knowing the geometry of the vehicle, and very few measurements, viz. flapping frequency and wing flap angle or timing of each cycle. The model also allows for reasonable estimates to be made for inbetween positions in the wake, where no direct measurements were available, thus providing more flexibility, for instance facilitating the use of blade element approaches to compute the tail forces. However, as the flapping-wing wake is unsteady, further analysis may be advisable to confirm what is happening at unobserved positions in the wake. With the available data, the current model provides an effective starting point to represent the wake in a realistic

but manageable way.

VI. Tail force modelling

VI.A. Effective velocity and angle of attack on the tail

The flapping-induced flow velocity models developed can be used within a blade element model of the tail aerodynamics. For this it is necessary to determine the specific velocities experienced along the tail leading edge. Fig. 4 shows the planform of the test platform tail. The developed wake model allows for the local induced velocities to be determined anywhere along the tail leading edge, as a function of instantaneous flap phase and spanwise and chordwise position of the point considered. The averaging introduced in vertical direction accounts for small variations and inaccuracies in the nominal z_B positioning of the tail. The suggested model provides a continuous mathematical description of the entire wake in the relevant domain, hence it is possible to determine the induced u and w velocities at any point and consequently to define blade elements with an arbitrarily close spacing.

Assuming the vehicle is moving with a forward velocity V, hence is affected by a free-stream velocity V_∞, the body-frame u and w velocities experienced by a particular blade element, and resulting total velocity, are given by:

$$\hat{u}_{t,loc} = \hat{u}_i + V_\infty \cos\alpha_B \tag{17}$$

$$\hat{w}_{t,loc} = \hat{w}_i + V_\infty \sin\alpha_B \tag{18}$$

$$\hat{V}_{t,loc} = \sqrt{\hat{u}^2_{t,loc} + \hat{w}^2_{t,loc}} \tag{19}$$

where α_B is the body AOA, the subscript i indicates induced velocities, a hat superscript indicates model-estimated values, and variables without superscript are assumed to be known.

The local AOA and velocity experienced at each blade element can then be computed using Eq. III, and the lift force at each blade element can be determined using a differential formulation of Eq. 1,

$$dL_t = \frac{1}{2}\rho c_t(r)\hat{V}^2_{t,loc} C_{l,t}(\hat{\alpha}_{t,loc})dr \tag{20}$$

where r is the spanwise distance from the wing root to the middle of the considered blade element, and $c_t(r)$ is the tail chord at this position.

An analogous expression can be obtained for the drag force at the blade element. Given that each blade element has a different orientation, due to the time-varying flow, the local definition of lift and drag has a different orientation at each station. Hence, in order to integrate the local forces, the differential forces are first transformed to the body coordinate system, based on the local AOA at each blade element. Integrating these components then yields the contribution of the tail to the body-frame X and Z forces.

VI.B. Lift and drag coefficients

The remaining unknown in Eq. 20 is the lift coefficient (and analogously the drag coefficient). Several options can be considered for this parameter, starting from a simple linear theory approach, where $C_{l,t} = 2\pi\alpha_{t,loc}$. However, a perhaps more realistic alternative is to assume that as the tail experiences a time-varying flow, its lift and drag coefficients take the same form as is typically assumed for flapping wings,[?] i.e.,

$$C_{L,t} = C_l \sin 2\alpha_{t,loc} \tag{21}$$

$$C_{D,t} = C_{d0} \cos\alpha_{t,loc} + C_{d\pi/2} \sin\alpha_{t,loc} \tag{22}$$

where C_l, C_{d0} and $C_{d\pi/2}$ are constants. The main limitation of this formulation is that the constants in the above equations are vehicle-specific parameters that must be determined experimentally or somehow estimated. This poses a challenge for several reasons. On the one hand, flapping-wing vehicles are generally very small, so their tails generate very small forces that may be difficult to measure even with highly accurate force sensors. This makes it particularly difficult to carry out measurements on the tail alone. On the other hand, clamping the full FWMAV results in vibrations, especially in z_B direction, that are not observed in free flight[?] – a potential problem because this is the direction the tail is expected to contribute to most.

Hence, in order to make an initial, qualitative evaluation of the modelling approach, values from the flapping-wing literature were used (Ref. ?, Fig. 9 in Ref. ?). The aerodynamic coefficients were thus set to the following values: $C_l = 1$, $C_{d0} = 0.05$, $C_{d\frac{\pi}{2}} = 2$. A thorough validation will require more extensive wind tunnel testing and is left for future work.

VI.C. Tail force model preliminary results

Results were computed in four different forward flight conditions, chosen to correspond to conditions measured in free-flight.

Prior to the forces, it is useful to consider the effective AOA and velocity resulting at the tail from the proposed modelling approach. These values depend solely on the proposed wake model and do not require assumptions on the lift coefficient. It can be observed that the local AOA at the tail is lowered significantly by the velocity induced by the flapping wings, which leads to values within the typical linear regime of a flat plate for a significant part of the tail (up to $d_s \approx 50mm$). This may help to explain why the tail still generates forces even at angles of attack that are very clearly outside the range that leads to force generation on a flat plate. Additionally, this suggests that the highly simplified lift formulation (Eq. 1) may be acceptable for a first approximation, even though it cannot capture all effects.

The effective AOA increases as we move outwards along the tail leading edge, towards the tip of the tail, as shown in Fig. 17. This can be explained by the decreasing flapping-induced velocity in the same direction, which means that the AOA is closer to the AOA of the wings/body. A gradual phase advance can also be observed, with movement towards the tip. Moreover, the oscillatory component increases in the same direction (i.e., larger peaks), echoing the increased peaks particularly in w along the same direction.

With increasing forward velocity of the body, the same trends can be observed, but the peaks and troughs move closer together, leading to less variation in the time-varying component. This may be due to the smaller contribution of the free-stream velocity to the w-component at higher velocities. The mean local AOA increases at higher velocities, but not to a significant extent. While at higher forward velocities, the flapping-induced velocity becomes less important compared to the free-stream velocity, hence the mean local AOA should be closer to that of the body, at the same time the body is at a lower pitch attitude to begin with, so the overall effect is partly cancelled out. At very low forward velocities, on the other hand, some of the local AOA values are even temporarily negative, which is possible due to the w component of the induced velocity, which varies in direction, and during the flap cycle can reach similar magnitude to u.

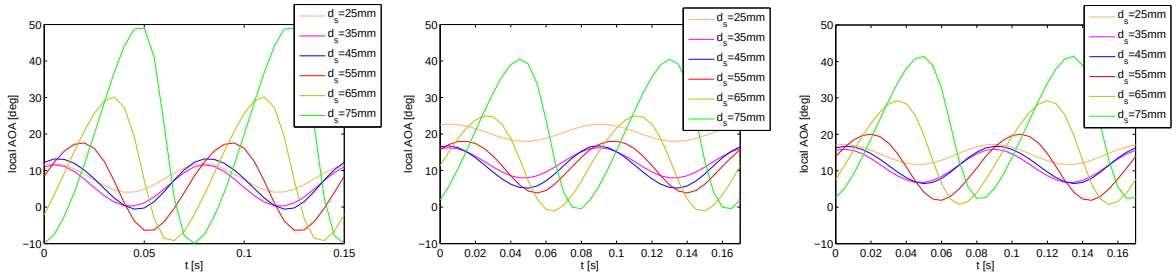

(a) $V_\infty = 0.3m/s$ (b) $V_\infty = 0.7m/s$ (c) $V_\infty = 1.0m/s$

Figure 17: Local angle of attack at different positions along the tail leading edge, for different free-stream velocities.

Initial results for the tail forces were obtained using the proposed aerodynamic coefficient formulations (Eqs. 21–22). At this stage, the results can mainly be evaluated qualitatively. Fig. 18 shows the resulting local lift coefficients at different blade elements along the tail leading edge – it can be observed that the coefficients become larger and advance in phase when moving outwards, while the peaks grow in amplitude, essentially replicating the trends in the local tail AOA. The mean lift coefficients also increase with increasing free-stream velocity, and the trend is more evident than in the AOA. It seems that at higher velocities, the effect of the larger free-stream experienced by the tail, due to the higher velocity and lower body pitch, dominates over the slight decrease in induced velocity from the wings.

The tail forces predicted by the suggested model are shown in Fig. 19. As expected, the contribution in x_B direction is minor (approximately 10 times smaller than in z_B direction), and tends to zero particularly at low forward velocities. The contribution to the Z force is more significant. While the values are small ($\sim 0.01 - 0.03N$), it should be considered that for the present platform this would constitute up to 20%

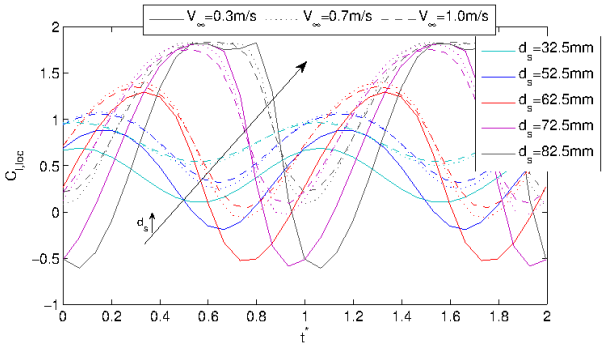

Figure 18: Local lift coefficient at different positions along the tail, for different free-stream velocities.

of the weight force (16g mass), and hence is not negligible. The signs are negative as expected, given that the tail would mainly produce a force upwards, i.e. in negative z_B direction. With increasing forward flight velocities, the tail produces more force, in an absolute sense, which reflects the free-stream effect.

While the values need to be validated using the actual aerodynamic coefficients of the test platform, their order of magnitude is plausible and remains similar if the aerodynamic coefficients are varied within the range typically encountered in the flapping-wing literature. Future work will encompass validation by means of tailed and tailless force balance measurements.[?]

Finally, it should be noted that the interaction between free-stream and wing wake is likely to be more complex than a simple addition, as an increasing free-stream velocity is likely to decrease the vorticity observed in the wake in hover conditions. This additional effect will be investigated in further work, however it requires experimental data in order to be confirmed and quantified.

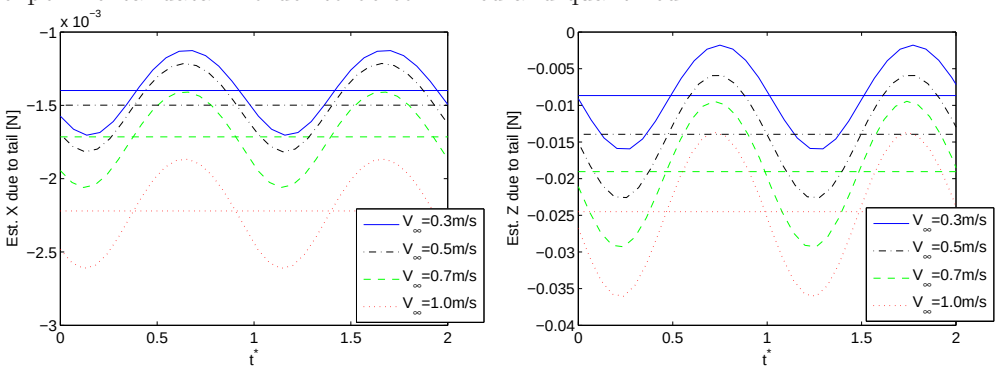

(a) X (b) Z

Figure 19: Preliminary tail force results, expressed in body frame, using aerodynamic coefficients from the literature.

VII. Conclusion

Tailed flapping-wing micro aerial vehicles have the advantage of having simpler mechanisms and control strategies than their tailless counterparts, particularly for hovering flight regimes. However, in the case of forward flight, the tail aerodynamics assume an important role in the control of the air vehicle. This study proposed a modelling approach based on novel multivariate simplex splines, to estimate the aerodynamic forces produced by the tail of a clap-and-peel flapping-wing vehicle during flight, under the influence of the wing wake. Particle image velocimetry (PIV) techniques were used to characteris the flow-field in the wake, as a function of spatial position and wing flap phase. After modelling the wake, the model output was validated by comparing the identified model to PIV data not used in the modelling process, revealing a significant accuracy. The obtained wake representation was then used to compute the aerodynamic forces acting on the tail using a standard aerodynamic model. This resulted in forces of a plausible order of magnitude when complemented with aerodynamic coefficients from the literature. However, despite being promising, the tail forces could not be validated due to the absence of reliable time-resolved force data. Future work will focus

of determining accurate tail forces and validating these, thus closing the research loop. A combination of the resulting model with a model of the flapping wings has the potential of fully representing the studied vehicle, constituting a useful basis for development of a full simulation framework, and supporting novel controller development.

Acknowledgements

The authors would like to thank Dr Mustafa Perçin for sharing and explaining the PIV measurements from his experiments.

References

[1]Keennon, M., Klingebiel, K., Won, H., and Andriukov, A., "Development of the Nano Hummingbird: A tailless flapping wing micro air vehicle," *50th AIAA Aerospace Sciences Meeting 09-12 January 2012, Nashville, Tennessee*, No. January, 2012, pp. 1–24.

[2]Ma, K., Chirarattananon, P., Fuller, S., and Wood, R., "Controlled Flight of a Biologically Inspired, Insect-Scale Robot," *Science*, Vol. 340, No. 6132, 2013, pp. 603–607.

[3]Gaissert, N., Mugrauer, R., Mugrauer, G., Jebens, A., Jebens, K., and Knubben, E. M., *Towards Autonomous Robotic Systems: 14th Annual Conference, TAROS 2013, Oxford, UK, August 28–30, 2013, Revised Selected Papers*, chap. Inventing a Micro Aerial Vehicle Inspired by the Mechanics of Dragonfly Flight, Springer Berlin Heidelberg, Berlin, Heidelberg, 2014, pp. 90–100.

[4]de Croon, G. C. H. E. D., de Clercq, K. M. E. D., Ruijsink, R., Remes, B., de Wagter, C., and Croon, G. C. H. E. D., "Design, aerodynamics, and vision-based control of the DelFly," *International Journal of Micro Air Vehicles*, Vol. 1, No. 2, 2009, pp. 71–98.

[5]Zdunich, P., Bilyk, D., MacMaster, M., Loewen, D., DeLaurier, J., Kornbluh, R., Low, T., Stanford, S., and Holeman, D., "Development and Testing of the Mentor Flapping-Wing Micro Air Vehicle," *Journal of Aircraft*, Vol. 44, No. 5, Sept. 2007, pp. 1701–1711.

[6]Pornsin-Sirirak, T. N., Tai, Y.-C., Ho, C.-M., and Keennon, M., "Microbat: A Palm-Sized Electrically Powered Ornithopter," *Proceedings of NASA/JPL Workshop on Biomorphic Robotics*, 2001, pp. 14–17.

[7]Hsu, C.-K., Evans, J., Vytla, S., and Huang, P., "Development of flapping wing micro air vehicles - design, CFD, experiment and actual flight," *48th AIAA Aerospace Sciences Meeting Including the New Horizons Forum and Aerospace Exposition*, 2010.

[8]Ellington, C. P., "The Aerodynamics of Hovering Insect Flight. I. The Quasi-Steady Analysis," *Philosophical Transactions of the Royal Society B: Biological Sciences*, Vol. 305, No. 1122, Feb. 1984, pp. 1–15.

[9]Sane, S. P. and Dickinson, M. H., "The aerodynamic effects of wing rotation and a revised quasi-steady model of flapping flight." *The Journal of experimental biology*, Vol. 205, No. Pt 8, April 2002, pp. 1087–96.

[10]Berman, G. J. and Wang, Z. J., "Energy-minimizing kinematics in hovering insect flight," *Journal of Fluid Mechanics*, Vol. 582, June 2007, pp. 153–168.

[11]Nakata, T., Liu, H., and Bomphrey, R. J., "A CFD-informed quasi-steady model of flapping-wing aerodynamics," *Journal of Fluid Mechanics*, Vol. 783, 11 2015, pp. 323–343.

[12]Armanini, S. F., Caetano, J. V., de Croon G. C. H. E., de Visser, C. C., and Mulder, M., "Quasi-Steady Aerodynamic Model of Clap-and-Fling Flapping MAV and Validation using Free-Flight Data," *Bioinspiration & Biomimetics*, Vol. 11, 2016, pp. 046002.

[13]Caetano, J. V., de Visser, C. C., de Croon, G. C. H. E., Remes, B. D. W., de Wagter, C., Verboom, J. L., and Mulder, M., "Linear Aerodynamic Model Identification of a FlappingWing MAV Based on Flight Test Data," *International Journal of Micro Air Vehicles*, Vol. 5, No. 4, December 2013, pp. 273–286.

[14]Grauer, J. and Jr, J. H., "Modeling of Ornithopter Flight Dynamics for State Estimation and Control," 2010, pp. 524–529.

[15]Armanini, S. F., Visser, C. C. D., Croon, G. C. H. E. D., and Mulder, M., "Time-varying model identification of flapping-wing vehicle dynamics using flight data," *Journal of Guidance, Control, and Dynamics*, Vol. 39, No. 3, 2016, pp. 526–541.

[16]Finio, B. M., Perez-Arancibia, N. O., and Wood, R. J., "System identification and linear time-invariant modeling of an insect-sized flapping-wing micro air vehicle," *2011 IEEE/RSJ International Conference on Intelligent Robots and Systems*, Ieee, Sept. 2011, pp. 1107–1114.

[17]Chand, A. N., Kawanishi, M., and Narikiyo, T., "Parameter Estimation for the Pitching Dynamics of a Flapping-Wing Flying Robot," *IEEE International Conference on Advanced Intelligent Mechatronics (AIM)*, Busan, Korea, 2015, pp. 1552–1558.

[18]Armanini, S. F., de Visser, C. C., and de Croon, G. C. H. E., "Black-box LTI modelling of flapping-wing micro aerial vehicle dynamics," *AIAA Atmospheric Flight Mechanics Conference*, Kissimee, FL, USA, Jan. 2015, AIAA Paper 15-0234.

[19]Grauer, J., Ulrich, E., Jr., J. H., Pines, D., and Humbert, J. S., "Model Structure Determination of an Ornithopter Aerodynamics Model from Flight Data," No. 2010-41, AIAA, January 2010.

[20]Percin, M., Eisma, H., van Oudheusden, B., Remes, B., Ruijsink, R., and de Wagter, C., "Flow Visualization in the Wake of the Flapping-Wing MAV 'DelFly II' in Forward Flight," *AIAA Applied Aerodynamics Conference*, AIAA, 2012.

[21]Muijres, F. T., Spedding, G. R., Winter, Y., and Hedenström, A., "Actuator disk model and span efficiency of flapping flight in bats based on time-resolved PIV measurements," *Exp. Fluids*, Vol. 51, 2011, pp. 511–525.

[22]Shkarayev, S. and Silin, D., "Applications of Actuator and Disk Theory and to Membrane and Flapping Wings," *AIAA Journal*, Vol. 48, No. 10, 2010.

[23]de Croon, G. C. H. E., Perçin, M., Remes, B. D. W., Ruijsink, R., and De Wagter, C., *The DelFly Design, Aerodynamics, and Artificial Intelligence of a Flapping Wing Robot*, Springer Netherlands, 2016.

[24]Percin, M., *Aerodynamic Mechanisms of Flapping Flight*, Ph.D. thesis, TU Delft, 2015.

[25]Oppenheimer, M. W., Doman, D. B., and Sigthorsson, D. O., "Dynamics and Control of a Biomimetic Vehicle Using Biased Wingbeat Forcing Functions," *Journal of Guidance, Control, and Dynamics*, Vol. 34, No. 1, Jan. 2011, pp. 204–217.

[26]de Visser, C., Chu, Q., and Mulder, J., "A new approach to linear regression with multivariate splines," *Automatica*, Vol. 45, No. 12, Dec. 2009, pp. 2903–2909.

[27]de Visser, C. C., *Global Nonlinear Model Identification with Multivariate Splines*, Ph.D. thesis, Delft Universitiy of Technology, 2011.

[28]Berman, G. J. and Wang, Z. J., "Energy-minimizing kinematics in hovering insect flight," *Journal of Fluid Mechanics*, Vol. 582, 2007, pp. 153–168.

[29]Caetano, J. V., Percin, M., van Oudheusden, B. W., Remes, B. D. W., de Wagter, C., de Croon, G. C. H. E., and de Visser, C. C., "Error Analysis and Assessment of Unsteady Forces Acting on a Flapping Wing Micro Air Vehicle: Free-Flight versus Wind Tunnel Experimental Methods," *Bioinspiration & Biomimetics*, Vol. 10, No. 5, 2015.

[30]Sane, S. P., "The aerodynamics of insect flight," *Journal of Experimental Biology*, Vol. 206, No. 23, Dec. 2003, pp. 4191–4208.